Research Article | Vol. 27, No. 9 | 29 Apr 2019 | OPTICS EXPRESS 12025
Optics EXPRESS

Optical diagnostic methods for monitoring the poling of thin-film lithium niobate waveguides

JIE ZHAO,* MICHAEL RÜSING, AND SHAYAN MOOKHERJEA

Department of Electrical and Computer Engineering, University of California, San Diego, 9500 Gilman Drive, Mail Code 0407, La Jolla, CA 92093-0407, USA
jiz378@eng.ucsd.edu

Abstract: We demonstrate two non-destructive methods of studying the gradual poling of thin-film lithium niobate waveguides by the application of a sequence of high-voltage pulses, and we show the transition from under-poling to over-poling and the identification of the optimal stopping point of the poling process. The first diagnostic method is based on changes in continuous-wave light transmission through a hybrid waveguide as it is gradually poled by using a second set of monitoring electrodes fabricated alongside the principal poling electrodes. The second method is based on confocal back-reflected second-harmonic microscopy by using femtosecond optical probe pulses. The results from the two methods are in agreement with each other and may be useful as non-destructive in situ diagnostic methods for optimized poling of integrated waveguides.

1. Introduction

Periodically-poled lithium niobate (PPLN), which can achieve quasi-phase matching (QPM) of nonlinear interactions between different wavelengths beyond the limitations and complexities of Type-I and Type-II phase-matching in LN, is used to realize waveguide devices that are useful in quantum communication [1, 2], optical parametric oscillators [3–5], and wavelength converters [6, 7]. Further improvements in performance are anticipated when using thin-film lithium niobate (TFLN), which achieves a smaller mode cross-sectional area, and thus, higher nonlinear conversion efficiency, compared to diffused or proton-exchanged LN waveguides. Thus, high-fidelity periodic poling of thin-film lithium niobate (TFLN) will be essential for efficient integrated nonlinear optical devices using the TFLN materials platform, which are recently being studied [8–13].

Periodic poling of lithium niobate (LN) is achieved by the application of a strong electric field to the crystal through lithographically-defined electrodes on LN surfaces. The electrodes are fabricated in a periodic pattern, which creates a periodic reversal of the ferroelectric domain orientation, and the resulting periodicity of the nonlinear polarization achieves a crystal momentum that assists in phase-matching of waves that would normally not interact. At the microscopic level, uniform and accurately-sized periodically-inverted domains are the sign of high poling quality. Perhaps the most popular conventional way to evaluate poling quality is one based on selective HF etching [14], but the process is difficult to control in thin LN films, and especially in hybrid devices which include materials, such as silicon dioxide, which are themselves etched by HF. Moreover, the process of HF etching also damages the LN waveguide itself, and is not a method that can be used for in-process diagnostics of the same waveguide. Thus, there is need to develop diagnostic methods for studying the poling characteristics of TFLN devices, and in particular, in-situ methods that do not destroy the waveguide or the surrounding materials.

Other methods of investigating the domain structures are second harmonic (SH) microscopy [15–18], and piezo-response force microscopy (PFM) [19, 20]. As shown so far, in-situ second harmonic generation (SHG) measurement [21, 22] requires knowledge of the phase matching

#359477 https://doi.org/10.1364/OE.27.012025
Journal © 2019 Received 4 Feb 2019; revised 28 Mar 2019; accepted 28 Mar 2019; published 15 Apr 2019

Optics EXPRESS

conditions before poling. Missey et al. [23] and Grilli et al. [24] have presented in-situ visualization of the domain formation process in bulk LN, while the demonstrated resolution was on the order of tens of microns. Karlsson et al. [25] developed a real-time poling monitoring technique, based on the electro-optic effect in ferroelectric crystals. This technique has been successfully demonstrated in the poling process of bulk KTP and RTP [25–27]. However, poling monitoring of TFLN has not yet been presented.

Here, we demonstrate poling diagnostic methods using hybrid TFLN devices, formed by bonding of unetched x-cut lithium niobate on insulator (LNOI) dies to patterned and planarized silicon photonic dies which have rib waveguide features. The thickness of the LN layer was 600 nm and of the Si layer was about 150 nm; the width of the Si rib was 320 nm and the lowest-order waveguide mode had an effective area of $A_{\text{eff}} \sim 1.13\ \mu\text{m}^2$. In contrast to etched TFLN waveguides, these multi-layer structures do not require etching of LN, and the bonding can be performed at room temperature, with a low-temperature anneal cycle, after the silicon photonic fabrication (e.g., at wafer scale, using cost-effect multi-process wafer fabrication runs) has been completed. In this way, integration of passive and active TFLN devices with integrated photonic components (e.g., tapers, splitters, combiners, couplers, etc.) formed entirely in other layers has already been shown [9, 28]. Here too, the rib features in this study were formed using silicon, which allows a convenient monitoring method using 1550 nm guided light which is sufficient for the present purposes. The hybrid waveguides provide lateral modal confinement solely by the rib feature patterned in the Si layer, while keeping most (75% and 85% for the fundamental TE and TM mode, respectively) of the (Poynting) power in the LN material. However, it should be noted that hybrid Si-LN waveguides are not suitable for usage at wavelengths shorter than about 1.1 microns; for those wavelengths, similar results may be obtained using hybrid silicon nitride, silicon carbide or other materials which can be bonded to LNOI. For this study and validation of the diagnostic methods, the poling period was chosen arbitrarily to be 5 μm, which is compatible with photolithography; other poling periods could be selected for a specific application e.g., difference frequency generation of infrared wavelengths, or parametric wavelength conversion.

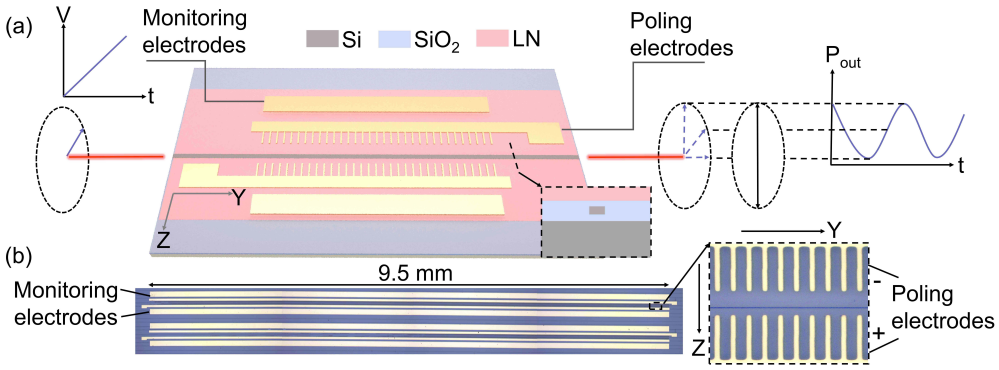

Fig. 1. (a) Schematic illustration of the poling monitoring process. Inset shows the not-to-scale cross-section of the hybrid Si-TFLN waveguide. (b) Top-view optical micrograph of the fabricated chip, which includes hybrid Si-TFLN waveguides and two sets of poling and monitoring electrodes.

2. Concept

A schematic illustration of the fabricated device is shown in Fig. 1(a), with the stitched microscope images of a fabricated device shown in Fig. 1(b). The TFLN waveguides were fabricated using the oxide-bonding process we have previously described in detail for ultra-high RF frequency

Optics EXPRESS

electro-optic modulators [28]. Two sets of electrodes, labeled poling and monitoring electrodes in Figs. 1(a) and 1(b), were fabricated by photolithography. In cross-section, the electrodes consist of a 10 nm Cr adhesion layer deposited on TFLN, followed by a 100 nm Au layer. For this study, we fabricated poling electrodes with a uniform 5 μm period, and with different duty cycles (the fraction of the period that is covered by Au) ranging from 25% to 50%. The separation gap between the two opposing electrode "teeth" facing each other (see inset of Fig. 1(b)) was defined by lithography to be 10 μm, based on an estimate of the critical field required for initiating poling (described further below). The center of the optical mode in the hybrid waveguide is placed closer to the positive poling electrodes, which allows the optical mode to see the most uniformly inverted region, based on insights in poling thin films [11]. Figure 2 depicts the simulated electric field distribution (using COMSOL) in the poling region with 400 V applied to the monitoring electrodes. As shown in Fig. 2(b), the optical mode (calculated by Lumerical Mode Solutions) sees relatively uniform electric field in both the poled and unpoled area during the monitoring steps.

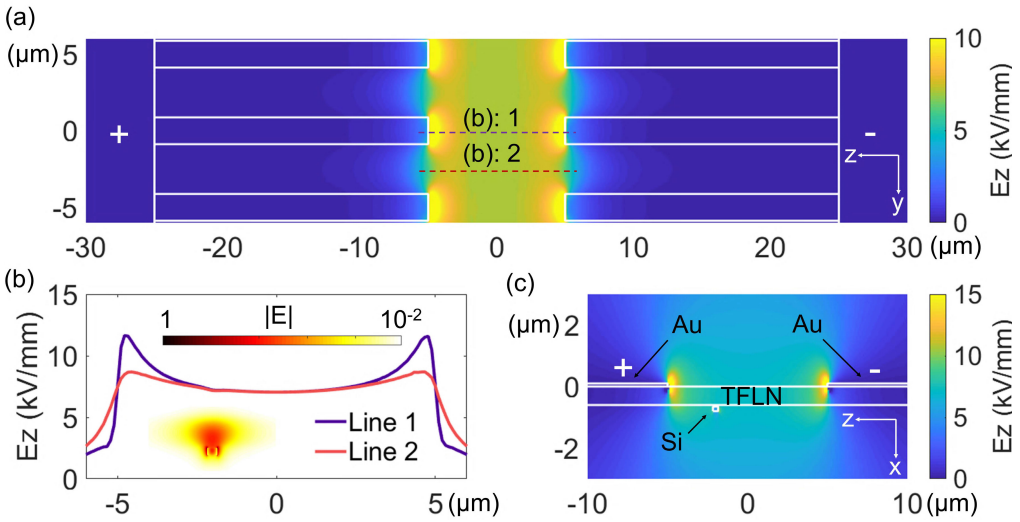

Fig. 2. Numerically simulated electric field distributions (all shown in E_z component) with 400 V applied to the monitoring electrodes (separated by 150 μm, not shown here). (a) E_z distribution in the y-z plane, at a slice through the middle of the TFLN region. The white solid lines indicate the edges of three pairs of poling electrodes, and the "+", "-" labels show the polarity of the electrodes. (b) E_z variation in the z direction along the two dashed lines shown in (a). Simulated E field intensity of the fundamental TE optical mode is overlayed in the plot, which shows the electrical field distribution seen by the optical mode. (c) E_z distribution in the x-z plane. The "+", "-" labels show the polarity of the electrodes.

Hybrid Si-TFLN waveguides were used to couple light into and out of the chip. Continuous-wave laser light at 1550 nm wavelength, polarized at 45° to the x and z axes of the TFLN microchip (see Fig. 1), was launched along the y axis, through the hybrid Si-TFLN waveguides. Tapered lensed fibers were used to couple light to the chip. When a voltage was applied to the electrodes (inducing an electric field along the z axis), the electro-optic effect rotates the output state-of-polarization (SOP) of the transmitted light. We quantified the change in the SOP by transmitting the light through a fiber-coupled polarizer and measuring the power on a photodiode. The voltage (linear) ramp was synchronized to the photodiode readout, so that the resulting waveform could be observed and interpreted as an "oscillation" (or lack thereof) of the recorded output light power (P_{out}) versus (probe) voltage.

Optics EXPRESS

Analytically, P_{out} depends on the total phase retardation between the x and z components of the light (Γ), and can be expressed as [26]:

$$P_{\text{out}} \propto (1 - \cos\Gamma), \tag{1}$$

where, in bulk LN, Γ is described by [26]:

$$\begin{aligned}\Gamma &= \frac{2\pi}{\lambda}(n_z - n_x)L + \frac{2\pi}{\lambda}E_z\left[\left(\frac{n_x^3}{2}r_{13} - \frac{n_z^3}{2}r_{33}\right)(L-x) - \left(\frac{n_x^3}{2}r_{13} - \frac{n_z^3}{2}r_{33}\right)x\right] \\ &= \frac{2\pi}{\lambda}(n_z - n_x)L + \frac{2\pi}{\lambda}E_z\left(\frac{n_x^3}{2}r_{13} - \frac{n_z^3}{2}r_{33}\right)(L-2x).\end{aligned} \tag{2}$$

E_z is the magnitude of the electric field applied for monitoring in the z direction, L is the total length of the poling region, x is the length of the inverted domains, $n_{\{x,\ z\}}$ is the refractive index in the x or z polarized direction, r_{13} and r_{33} are the electro-optic coefficients of LN, and λ is the wavelength of the input light. The poling duty cycle (ξ) is defined as $\xi = x/L \times 100\%$.

The physics of Eq. (2) describes the differential phase accumulation between the two interfering field components, which translate, in the context of TFLN waveguides, to the (quasi-) TE and TM polarized lowest-order modes. Thus, in our experiment,

$$\Gamma = \frac{2\pi}{\lambda}(n_{\text{eff}}^{\text{TE}} - n_{\text{eff}}^{\text{TM}})L + \frac{2\pi}{\lambda}\left\{\left[\Delta n_{\text{eff}}^{\text{TE}}(E_z) - \Delta n_{\text{eff}}^{\text{TM}}(E_z)\right](L-x) + \left[\Delta n_{\text{eff}}^{\text{TE}}(-E_z) - \Delta n_{\text{eff}}^{\text{TM}}(-E_z)\right]x\right\}, \tag{3}$$

where $\Delta n_{\text{eff}}^{\{\text{TE},\ \text{TM}\}}(\{E_z,\ -E_z\})$ is the fundamental TE or TM mode index change in the unpoled or poled region, respectively. Note that, here, the sign reversal of the electric field is equivalent to that of r_{13} or r_{33}, because $\Delta n_{\text{LN}}^{\{\text{TE},\ \text{TM}\}}(E_z) = -1/2n_{\{z,\ x\}}^3 r_{\{33,\ 13\}}E_z$, for the TE and TM polarizations, respectively.

In the case of unpoled bulk LN ($x = 0$), as one applies a linearly-increasing E field, i.e., a voltage ramp, the measured P_{out} would behave as $1 - \cos\{\Gamma' + \Gamma[E_z(t)]\}$, where Γ' and $\Gamma[E_z(t)]$ are the phase differences caused by the modal dispersion and the electro-optic effect, respectively. During poling, the oscillation gradually disappears as ξ increases from 0 up to 50%, and then appears again as the poling duty cycle increases further. This is because the phase retardation in the inverted and uninverted domains will be mutually cancelled out if $L = 2x$ (i.e., duty cycle = 50%), which results in $\Gamma[E_z(t)] = 0$.

In the hybrid Si-TFLN waveguides, $\Delta n_{\text{eff}}^{\{\text{TE},\ \text{TM}\}}(E_z) \neq -1/2n_{\{z,\ x\}}^3 r_{\{33,\ 13\}}E_z$. Therefore, we used a finite-difference eigenmode solver to simulate the waveguide cross-section and calculate the effective indices. (Our previous work has verified the accuracy of these models [9].) Figure 3(a) depicts the cross section of the hybrid Si-TFLN waveguide used in the simulations. The axial components of the calculated Poynting vector (i.e., along the propagation direction) for the fundamental (quasi-) TE and TM lowest-order modes are shown in Fig. 3(b). The hybrid waveguides are designed so that the optical mode is laterally confined in the Si waveguide while most (75% and 85% for TE and TM mode, respectively) of the power resides in the LN region. Such a structure provides a nearly linear relationship between the mode refractive index variation and the applied electric field in the hybrid Si-TFLN waveguide, which is very similar to that of the bulk LN (see Fig. 3(c)). Therefore, when exactly half of the sample is poled, we expect that the measured monitoring signal will be almost flat as a function of the monitoring voltage, the same behavior as seen in bulk LN (see Fig. 3(d)). The slight nonlinearity of Δn_{eff} with respect to E_z in Fig. 3(c) is because the portion of light confined in the LN region, relative to the surrounding materials, changes with the applied voltage. However, this effect is minor, and the trend shown in Fig. 3(c) appears linear, for all practical purposes.

Optics EXPRESS

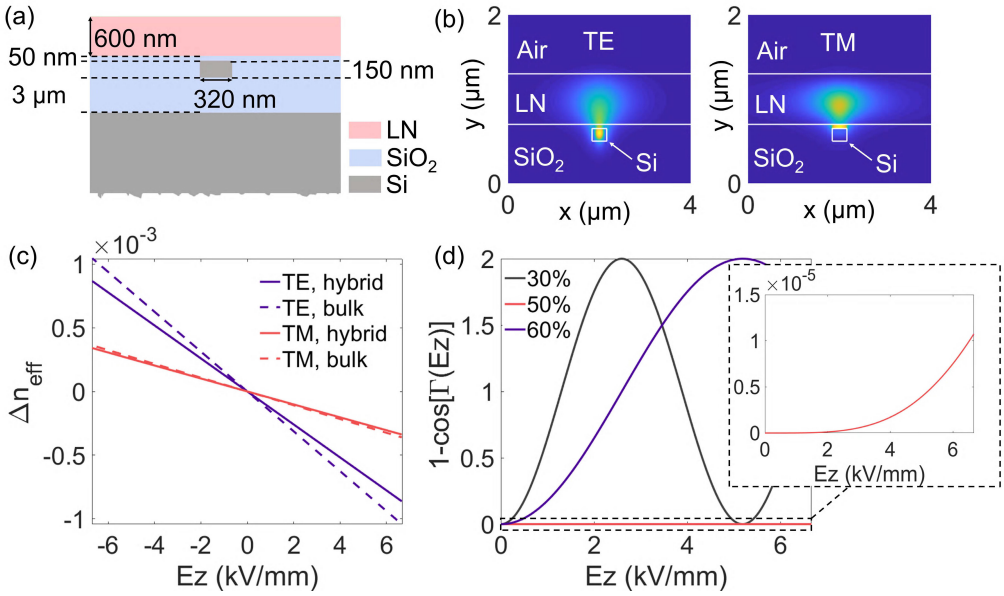

Fig. 3. (a) Not-to-scale schematic cross section of the hybrid Si-TFLN waveguide. (b) Simulated TE and TM mode Poynting vector components along the direction of propagation at 1550 nm. (c) Calculated TE and TM mode refractive index variation as a function of the applied electric field in hybrid Si-TFLN waveguides (solid line) and bulk LN (dashed line). (d) Calculated 1-cos[$\Gamma(E_z)$] as a function of the applied electric field with different poling duty cycles.

3. Method

3.1. *Bonded TFLN poling and monitoring*

The voltages required for poling TFLN are generally less than 1 kV, which is much smaller than for poling conventional LN waveguides. No special holder was required; however the device was poled with transformer oil surrounding the probe-pad contact point and the immediate vicinity of the electrodes along the entire length of the waveguide, which helped prevent arcing and electrode breakdown. We applied a sequence of 500 V or 600 V pulses to the poling (electrical) circuit using a high voltage amplifier (HVA) as shown in Fig. 4(a). We choose a commonly-used poling voltage waveform (see Fig. 6(a)), i.e. a rapid ramp-up of the poling voltage to a value higher than voltage required to exceed the coercive field strength (here, calculated to be about 210 V), which initiates the generation of nucleation sites, followed by a slow ramp-down of the poling voltage, which stabilizes the newly-formed domains (in analogy with the known mechanisms in bulk LN [29]).

The optical monitoring technique was included as part of the poling setup, as shown in Fig. 4(a), which allows diagnostics of poling without removing the chip from the setup. A linearly-increasing voltage waveform i.e., a ramp, with a minimum at 0 V and a maximum at 400 V over 50 s was applied to the monitoring electrodes, and the output light power was recorded by a multimeter. Traces were recorded before poling was initiated, and were also recorded after each poling pulse. By comparing the magnitude and number of oscillations in the measured monitoring signals, we can infer how much of the LN has been poled; the oscillations (as a function of probe voltage) are expected to nearly completely disappear when exactly one-half of the LN is poled, and are expected to be clearly evident both for under-poling and for over-poling. In principle, the monitoring process can be performed while poling the samples, for a true in-situ

measurement, as shown in references [25–27]. However, we choose to separate the monitoring and poling process in our experiment, in order to quantify the poling results.

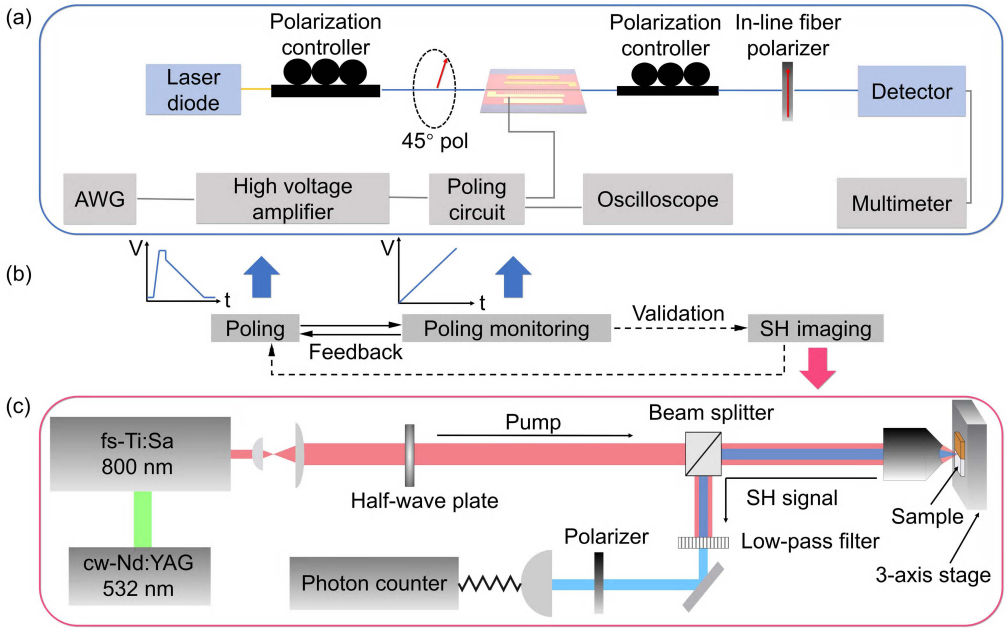

Fig. 4. Schematic illustrations of the poling and poling monitoring setup (a), measurement process (b), and the SH microscopy setup (c).

3.2. *Domain structure visualization*

As an integral method, the optical transmission monitoring technique provides us the poling information path-averaged along the entire hybrid waveguide structure, but it can not resolve the local inhomogeneities of the inverted domains in thin-film lithium niobate. To supplement these measurements, we performed second harmonic microscopy to gain some insights in the local texture of individual domain structures of the hybrid TFLN waveguides. The setup is shown in Fig. 4(c). The technique makes use of the fact that the SH generation observed in back-reflection (i.e., in the absence of any user-induced phase-matching) upon surface illumination using femtosecond optical pulses is highly sensitive to local changes in crystal structure and symmetry. Previously, this technique has been used to visualize domain structures in thin-film and bulk LN [15–18, 30–32]. In our setup, a femtosecond Ti:Sapphire (95 MHz repetition rate, < 100 fs pulse length, 25 mW focused power) operating at around 800 nm wavelength was focused, via an infinity corrected objective lens (NA = 0.55), on the sample surface. Depending on the nonlinear properties in the focus region, second-harmonic light (around 400 nm wavelength) is generated, which was collected in back-scattering mode using the same objective. The reflected pump light was blocked by a dichroic beam-splitter and band-pass filters. The filtered SH light was detected by a single-photon avalanche diode (SPAD) connected via a single-mode optical fiber with a 2.4 μm core diameter, which also served as the confocal pinhole. The optical system provides in vacuum a lateral resolution of about 400 nm and an axial (depth) resolution of about 2000 nm. It should be noted, that the depth resolution and to a lesser degree the lateral resolution deteriorates, when focusing into refracting media [33]. For our experiment this is of no concern, as these effects start to become noticeable, when focusing tens of microns below interfaces. However, in our experiment we are investigating the TFLN layer exposed at the surface, which in any case is

thinner than the depth resolution. Due to the confocal configuration, scanning of the sample, rather than the beam, was performed in order to generate a "map" of the domain structure. To achieve this, the sample was mounted on a 3-axis piezo-stage and scanned, whereas the optical beam maintained a fixed focus point. In order to create a typical 2D image, a selected region was scanned with 100 nm step width along the y and z axes of the TFLN, and 10 ms signal integration time per acquisition point. Please note, that the step width is chosen to be smaller than the optical resolution to acquire an image with a resolution limited by the optical setup rather the step size. In these experiments, the chip was removed and replaced, in order to image the gradual growth of the inverted domains after each poling pulse, while the scanned area was kept the same. Exact re-positioning of the sample was not achieved, resulting in some mis-alignment in the visual appearance of successive traces, as evident in Fig. 6(c). These do not significantly affect either the results or the interpretation.

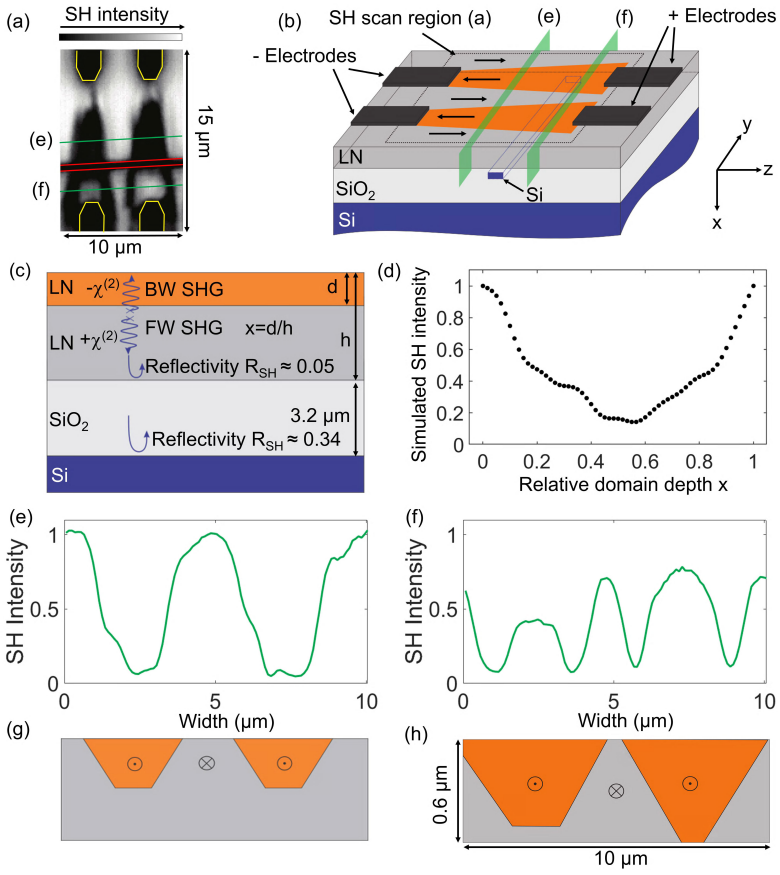

Fig. 5. (a) Typical SH microscopy scan result of a poled sample. For clarity the waveguide and electrodes are highlighted in red and yellow, respectively. (b) Sketch of the imaging and domain geometry of the scanned region in (a). Poled regions are marked in orange, while unpoled lithium niobate is colored in gray. (c) Not-to-scale cross-section of the sample highlighting the involved processes, i.e. BW SHG, FW SHG and reflections at the interfaces. (d) Simulated SH signal for a varying relative domain depth x. (e)-(f) Line scans of the nonlinear signal taken along the lines highlighted in (a). (g)-(h) Sketches of the suggested depth profile of the domains estimated from the simulation results in (d).

Figure 5(a) shows an as-measured second harmonic image taken around two electrode pairs

Optics EXPRESS

after applying four consecutive poling pulses to the sample, as shown in Fig. 6(a). For comparison Fig. 5(b) shows a simplified sketch of this region highlighting the scan area in relation to main features. In this sketch, unpoled regions are colored in grey, while poled regions are colored in orange. Electric-field-driven ferroelectric domain reversal in LN is typically characterized in four steps [34]: (1) nucleation of new domains, (2) axial growth along the z axis of the crystal, (3) lateral spread and growth in the x and y directions of the crystal and (4) coalescence of neighboring domains. Domain reversal in bulk and thin-film LN is usually observed to start at the positive electrode [18, 35], which is traced back to the difference in Schottky barriers at polar surfaces in LN [36]. The nucleation probability of new domains scales exponentially with the applied field [29, 37]. Therefore, we expect domain nucleation to start only close to the positive electrode tips, which is also observed. The domain propagation speed is characterized by a pronounced asymmetry, where the growth in the axial direction is about two to three orders of magnitude larger, than the spread in the lateral direction. Domains in congruent lithium niobate typically grow in hexagonal cross sections in the x-y plane, with the y axis of the crystals pointing into the corners of the hexagon [35]. Therefore, we expect the newly-formed domains close to the positive electrodes to be broader, and gradually tapering down towards the negative electrodes, and we also expect a similar behavior along the vertical dimension (i.e., in depth), as indicated by the simplified sketches of the cross sections in Figs. 5(g) and 5(h).

As the sketch Fig. 5(b) suggests, the second harmonic image can be divided into three main sections: the electrodes, the unpoled, and the poled regions. Further, the Si waveguide is visible as a line with decreased, but nonzero intensity. For visibility it is highlighted by a red border. The electrodes, which are highlighted by yellow lines, provide no SH signal, as the metal is not transparent and has no $\chi^{(2)}$ nonlinearity at this wavelength. The unpoled regions of the TFLN provide a homogeneous SH signal level due to the intrinsic nonlinearity of LN. The poled regions feature the general trapezoid shape with a broader base close to the positive electrodes as described above, but an additional substructure with broad dark areas surrounding bright areas is also observed. To understand these observations, the contrast mechanism in the system needs to be considered. In general, the pump light will generate second harmonic generation in forward (FW), i.e. propagation in the same directions as the pump beam, or backward (BW) direction, as shown in Fig. 5(c). BW and FW generated SH light is characterized by different phase matching conditions and therefore coherence lengths for the SHG process (FW: $\Delta k = k_{SH} - 2k_f$; BW: $\Delta k = k_{SH} + 2k_f$ [17]). Taking the extraordinary refractive indices of lithium niobate at the pump and SH wavelength into account, this results in a coherence length of $l_{C,\,BW} \approx 44$ nm for BW scattering and $l_{C,\,FW} \approx 1275$ nm for FW scattering. If BW scattering is the only dominant process in SH microscopy of the TFLN, one will expect a dark contrast for two stacked domains of opposing direction almost independent of their relative thickness. This is similar to previous observations of stacked domains in a similar geometry, where reference beams [31] or reference samples [38] can be used to visualize domains or domain polarity, rather than domain walls. However, in the thin film geometry, the FW generated light will also be detected in the backward direction due to reflections at the LN/SiO_2 and SiO_2/Si interfaces. The SH intensity scales quadratically with the interaction length. The interaction length for FW generation is more than 10 times longer, than the coherence length of BW generation, and also is more than twice the thickness of the TFLN. Therefore the FW signal will be more than 2 orders of magnitude larger, compared to the BW generated SH light. Based on the refractive indices at 400 nm, the reflectivity at the interfaces can be estimated at 0.05 for the LN/SiO_2 interface, and up to 0.34 for the Si/SiO_2 interface, due to the high index of Si at 400 nm (up to 5.57) [39]. This presents an explanation for the large intensities, we observed in SH microscopy from the TFLN. The importance of reflected signal from the bottom layer, also can explain another observation in the data. Although the waveguide is below the layer, its presence is clearly visible by a drop in SH intensity in the scan, which can only be explained if light interaction with the layer below

Optics EXPRESS

the film contributes to the detected signal. Here, the only 320 nm wide waveguide will partly diffract, scatter and absorb the FW generated SH signal, leading to a reduction in intensity.

The coherence length for FW generated light is longer than the TFLN thickness. Therefore, the FW generated light can coherently and continuously interact over the complete thickness of the film. For a growing domain with thickness d (Fig. 5(c)), a continuously decreasing signal with a minimum at about half the film thickness may be predicted. This is consistent with our observation of a gradually decrease and increase of signals in the suspected partially poled regions. It should be noted that the sensitivity for the inversion depth is purely dependent on the coherent nature of the nonlinear process, and is at first order not dependent on the diffraction limited depth resolution of the optical system.

To confirm this prediction, we have modeled the nonlinear response for a partially poled film in back-reflection based on a model and code developed by Sandkuijl et. al. [40]. The model can describe the nonlinear response from an arbitrary $\chi^{(2)}$ distribution in a full three-dimensional focus calculation, as well as includes reflection from planar interfaces for fundamental and SH light treated in a transfer matrix formalism. For more details on the code and calculation methodology, the original work by Sandkuijl et. al. [40] should be concerned. In our calculation we assume a numerical aperture of 0.55, illuminated with linear polarized plane waves. The polarization is aligned parallel to the z axis of LN and the focus is placed at the center of the LN layer. For simplification the $\chi^{(2)}$ of LN is only represented by a single tensor element d_{33}, which is similar to our experiment. Due to the used low order NA, the amount of non-x polarized components in the focus spot is minimal. The model includes a 600 nm film of lithium niobate on a 3.2 μm SiO_2 layer, with a silicon substrate, similar to our structure as shown in Fig. 3(a). The waveguide is currently not included in the model, as the calculation can only treat reflections between infinite interfaces orthogonal to the beam propagation. All materials are described with their respective refractive indices at the fundamental and SH wavelength (LN(e): $n_f = 2.1755$, $n_{SH} = 2.3321$; SiO_2: $n_f = 1.4533$, $n_{SH} = 1.4701$; Si: $n_f = 3.7$, $n_{SH} = 5.57$) [39,41,42]. In the simulation, the depth d of a domain with $-\chi^{(2)}$ is increased in 10 nm steps in the TFLN, as shown in Fig. 5(c), and the SH intensity collected by the objective in backscattering is calculated. The simulation result is normalized to the maximum intensity observed for a fully inverted ($x = 1$) or non-inverted ($x = 0$) domain. The result is depicted in Fig. 5(d) and shows a gradual decrease of the SH intensity to a minimum of 15% for a roughly 50% inverted film. The decrease is not symmetrical, which suggests a more complex interplay of reflections, resonant enhancements or phase matching. The weak oscillations, for example, are consistent with a period of about 90 nm hinting a BW phase-(mis)-matched process being responsible for parts of the signal. The simulation suggests that SH microscopy may be able to detect the inversion depth non-destructively and with high resolution, i.e. line scans as displayed in Figs. 5(e) and 5(f), may be interpreted as partly inverted films as in Figs. 5(g) and 5(h). However, for a more conclusive answer, a more detailed investigation of this process is required, e.g. understanding the effects of film thicknesses, handle materials and limits of this method, which is beyond the scope of this work.

4. Results and discussion

The measured poling voltage and current waveforms are shown in Fig. 6(a), the optical monitoring signals are shown in Fig. 6(b) and the domain-wall images using SH microscopy are shown in Fig. 6(c), after a certain number of poling pulses were applied. For these measurements, the length of the poling electrode was $L = 0.95$ cm, with 5 μm period and 35% duty cycle. Four 500 V and twelve 600 V pulses were applied to this sample in total. However, not all the applied pulses made notable contributions to the poling process, which will be explained further below. The TFLN used in this experiment was commercially acquired (NanoLN, Jinan Jingzheng Electronics Co., Ltd.) and is single-domain film before poling.

Optics EXPRESS

As shown in Fig. 6(a), a large current spike was measured during the first voltage pulse, which suggests most of the nucleation cites have been generated near the electrode that carries the positive charge. The recorded monitoring signal (Fig. 6(b), solid red line) shows fewer oscillations compared to what was measured before poling (Fig. 6(b), solid purple line). This suggests that some of the domains have propagated, upon application of the poling pulses, to the physical region of the LN film where the optical mode sits. This agrees well with the SH images shown in Fig. 6(c), where red and yellow solid lines were added manually to outline the Si waveguides and the poling electrodes respectively.

After the fourth poling pulse, the oscillations in the monitoring signal further decrease, which suggests that the poled area grew more into a region shared with the optical mode; this is confirmed by the SH image. We observed a decrease in the poling voltage on the sample after the first poling pulse, when keeping the output voltage from the high-voltage amplifier constant at 500 V. This may be because the generation of domain walls may have increased the conductivity of the TFLN [43,44]. This may also explain why we did not observe a noticeable domain growth in the z direction until we increased the poling voltage from 500 V up to 600 V. Oscillations in the monitoring signal almost disappeared after the sixth poling pulse, which indicates the desired end-point of the poling process at which about one-half of the LN region, as sampled by the guided optical mode itself, has been poled. Note that this does not mean that the poling duty cycle is 50% everywhere, and indeed, the SH image of a certain portion of the waveguide shows that the area near the positive electrodes is slightly overpoled, while the other side stays underpoled. For this experiment, we proceeded to pole further, and as expected, the oscillations are once again clearly measured. This demonstrates the usefulness of the optical monitoring method in non-destructively measuring the poling characteristics of TFLN waveguides.

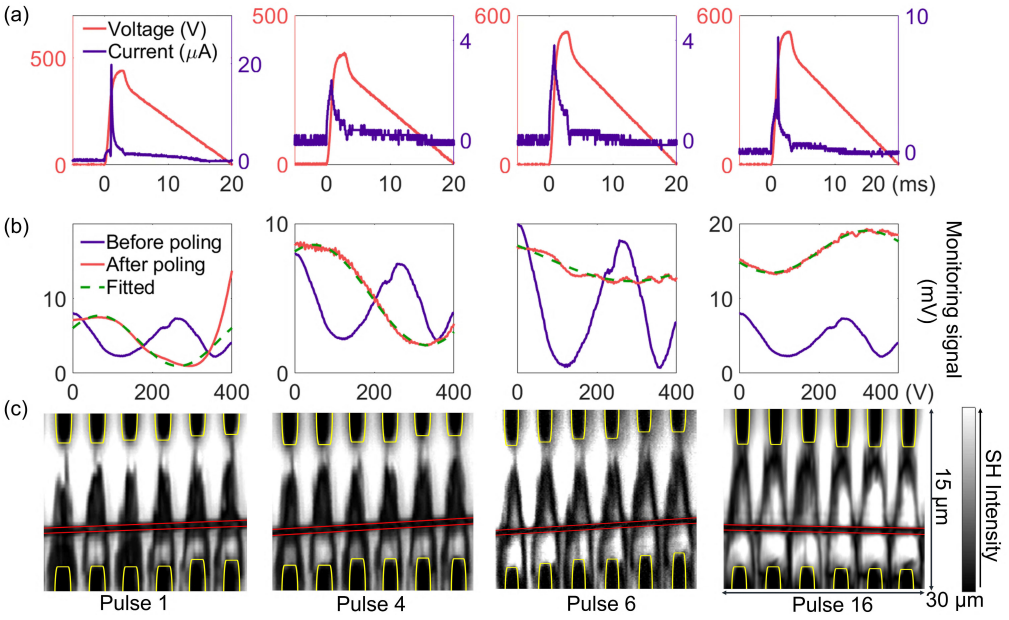

Fig. 6. (a) Measured poling voltage and current waveforms. (b) Recorded poling monitoring signals. (c) Second-harmonic confocal microscope images, after the indicated number of poling pulses were applied.

Here, to better evaluate the consistency of the two methods, we extract the poling duty cycle

Optics EXPRESS

(ξ) by fitting the measured monitoring signals, based on the following equation:

$$P_{\text{out}} = A \times (1 - \cos[\Delta\phi_{\text{in}}(\xi_{\text{m}}) + \Delta\phi(\xi_{\text{m}}) + \theta]) + C. \quad (4)$$

P_{out} is the recorded monitoring data, $\Delta\phi_{\text{in}}(\xi_{\text{m}})$ and $\Delta\phi(\xi_{\text{m}})$ are the phase differences between the TE and TM mode in the inverted and uninverted regions, assuming the poling duty cycle is ξ_{m}, which are calculated based on the simulation results from Eq. (3). The fitting parameters are A, θ, ξ_{m} and C. Note that to extract these parameters, we also need to know the actual electric field (E_{R}) in the monitoring region. Here, E_{R} was calculated by fitting the recorded monitoring signal before poling. A good agreement is obtained by setting $E_{\text{R}} = 3.5$ kV/mm in contrast with the simulated value $E_z \approx 7.2$ kV/mm (see Fig. 2(b)). This discrepancy may come from the differences in the actual waveguide structure and material properties compared to the assumptions made in the simulation, which did not take into account finite conductivity of the electrodes, imperfect contacts, or other sources of the voltage loss. In addition, 400 V was the output voltage from the HVA, the voltage applied on the sample is approximately 350 V. For the four poling pulses shown in Fig. 6, the predicted poling duty cycles are 20%, 29%, 64% and 75%. Substituting these parameters in Eq. (4), we were able to reproduce the measured monitoring signal after each poling pulse (Fig. 6(b), dashed green lines).

In agreement with the monitoring data, the nonlinear images in Fig. 6(c) show a gradual increase of the poled area after each pulse. A particular large increase can be seen at pulse 6 compared to the previous images, as the voltage was increased. Assuming this local SH image is representative of the complete device, the images can be used to estimate the poling duty cycles. We numerically define and calculate the poling duty cycles based on the SH images as

$$\xi_{\text{SH}} = \frac{A_{\text{O}} \cap A_{\text{in}}}{A_{\text{O}}} \times 100\%. \quad (5)$$

A_{O} is the area where the optical mode sits; this area was defined here as the geometrical rectangle that extends ± 2 μm from the center of the Si waveguide. A_{in} is the area that represents the inverted region, which is the area outlined by the boundaries of the inverted domains as identified by SH microscopy. This formula itself can provide an estimation of the duty cycle, if an area (that overlaps with the optical mode) is completely inverted, i.e. the measured SH signal level is similar to the unpoled regions, and a thin boundary to an uninverted region is observed. Note that, as is mentioned above, the prerequisite for applying Eq. (5) to the measured SH images is that the local SH image is representative of the entire structure, i.e. the uniformity of the poled regions is fairly good along the y axis of the TFLN. In our experiment, these conditions are satisfied only after the sixth voltage pulse, where all depicted inverted regions in the image show a comparable width and general appearance. In contrast to this, for the preceding pulses each inverted region has a unique shape, width and appearance, rather than a similar shape. For example after the first pulse, some areas around the waveguide have already been completely inverted as shown by the SH images, while other areas are only partly inverted and to a varying degree. Therefore, for the pulses before the sixth pulse, we can only estimate an effective duty cycle of less than 50% as an upper boundary, which is in agreement with our observations from the monitoring signals. The interpretation of the SH contrast mechanism, as explained in Sec. 3.2., suggests that it may be possible to extract an approximate depth of the inverted domain from the signal decrease of the SH signal level. This mechanism, combined with optimized poling recipe (better poling uniformity), might allow us to estimate an effective duty cycle for partly inverted structures. However, further investigations are necessary to understand the detailed mechanisms and influence of different parameters, such as the signal decrease due to the waveguide or oxide and TFLN thicknesses, which is beyond the scope of this work.

The SH images indicate the inhomogeneity of the inverted domains along the z axis. To improve the poling process further, there are a number of steps that could be taken. We conjecture

Optics EXPRESS

that poling homogeneity in the z direction can be improved by using a thin insulation layer to prevent domain spreading in the y direction [45]. Narrower poling electrodes, with a smaller duty cycle, in combination with shorter and higher poling pulses may also help in achieving uniform poling.

Figure 7 compares the ξ_m values with the calculated ξ_{SH} values, where ξ_m shows a clear transition from under-poling to over-poling. Despite the small areas of the SH scans, the results from the two methods are in agreement with each other, which indicates a comparable domain structure over the complete sample. SH images were not recorded after the eighth, nineth, or eleventh through fifteenth voltage pulses, because these pulses were applied consecutively, without stopping the experiment to remove and measure the microchip in the SH setup as previously observed changes were only minor.

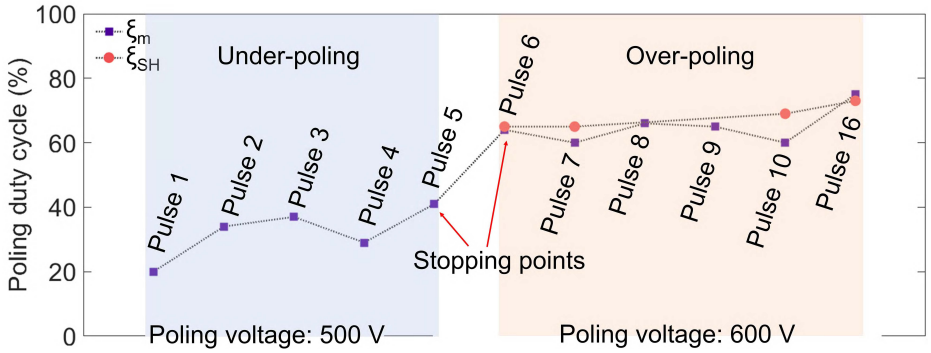

Fig. 7. Comparison of the predicted poling duty cycles (ξ_m) inferred from the recorded monitoring signals, and the calculated poling duty cycles (ξ_{SH}) based on the measured SH images.

5. Conclusion

In summary, we showed gradual poling of bonded hybrid TFLN waveguides using a series of voltage pulses between 500 V and 600 V, and we developed and demonstrated an electro-optical monitoring technique for suggesting the ideal end-point of the poling process, i.e., how many voltage pulses should be applied. Here, the predictions of the optical monitoring technique were validated by the second-harmonic images. This technique, combined with second harmonic microscopy can provide us both local and global information of the poling results, and thus yield useful data that may improve the tailored development of optimized poling recipes and improved device structures. This technique can also be used together with conventional monitoring techniques such as readout of the voltage and current characteristics, and second harmonic generation measurements. Additionally, in contrast with HF-etching based diagnostics, all of these methods are non-destructive. We believe the techniques and results presented here will benefit and accelerate the development of integrated quasi-phase-matched structures in integrated photonics incorporating thin-film lithium niobate.

Funding

Sandia National Laboratories (SIGMA-NONLin Project); National Science Foundation (NSF) (EFMA-1640968).

Optics EXPRESS

Acknowledgments

The authors would like to thank Peter O. Weigel for designing the silicon photonic structures and assisting with the bonding process. The authors are grateful to Anthony Lentine, Douglas Trotter, Dana Hood, John Mudrick, Christina Dallo, Andrew T. Pomerene, Andrew L. Starbuck, and Christopher T. DeRose of Sandia National Laboratories, Applied Microphotonic Systems, Albuquerque, New Mexico, 87185, USA, for collaboration on the fabrication of silicon photonic structures.

References

1. S. Tanzilli, W. Tittel, H. De Riedmatten, H. Zbinden, P. Baldi, M. Demicheli, D. B. Ostrowsky, and N. Gisin, "PPLN waveguide for quantum communication," Eur. Phys. J. D **18**, 155–160 (2002).
2. S. Tanzilli, W. Tittel, M. Halder, O. Alibart, P. Baldi, N. Gisin, and H. Zbinden, "A photonic quantum information interface," Nature **437**, 116–120 (2005).
3. L. E. Myers, R. C. Eckardt, M. M. Fejer, R. L. Byer, W. R. Bosenberg, and J. W. Pierce, "Quasi-phase-matched optical parametric oscillators in bulk periodically poled LiNbO3," J. Opt. Soc. Am. B **12**, 2102–2116 (1995).
4. S. D. Butterworth, V. Pruneri, and D. C. Hanna, "Optical parametric oscillation in periodically poled lithium niobate based on continuous-wave synchronous pumping at 1.047 microm," Opt. Lett. **21**, 1345–1347 (1996).
5. L. Lefort, K. Puech, S. D. Butterworth, G. W. Ross, P. G. Smith, D. C. Hanna, and D. H. Jundt, "Efficient, low-threshold synchronously-pumped parametric oscillation in periodically-poled lithium niobate over the 1.3 μm to 5.3 μm range," Opt. Commun. **152**, 55–58 (1998).
6. K. R. Parameswaran, J. R. Kurz, R. V. Roussev, and M. M. Fejer, "Observation of 99% pump depletion in single-pass second-harmonic generation in a periodically poled lithium niobate waveguide," Opt. Lett. **27**, 43–45 (2002).
7. R. V. Roussev, C. Langrock, J. R. Kurz, and M. M. Fejer, "Periodically poled lithium niobate waveguide sum-frequency generator for efficient single-photon detection at communication wavelengths," Opt. Lett. **29**, 1518–1520 (2004).
8. L. Chen, Q. Xu, M. G. Wood, and R. M. Reano, "Hybrid silicon and lithium niobate electro-optical ring modulator," Optica **1**, 112–118 (2014).
9. P. O. Weigel, M. Savanier, C. T. DeRose, A. T. Pomerene, A. L. Starbuck, A. L. Lentine, V. Stenger, and S. Mookherjea, "Lightwave circuits in lithium niobate through hybrid waveguides with silicon photonics," Sci. Reports **6**, 22301 (2016).
10. L. Chang, M. H. P. Pfeiffer, N. Volet, M. Zervas, J. D. Peters, C. L. Manganelli, E. J. Stanton, Y. Li, T. J. Kippenberg, and J. E. Bowers, "Heterogeneous integration of lithium niobate and silicon nitride waveguides for wafer-scale photonic integrated circuits on silicon," Opt. Lett. **42**, 803–806 (2017).
11. L. Chang, Y. Li, N. Volet, L. Wang, J. Peters, and J. E. Bowers, "Thin film wavelength converters for photonic integrated circuits," Optica **3**, 531–535 (2016).
12. A. Rao and S. Fathpour, "Second-harmonic generation in periodically-poled thin film lithium niobate wafer-bonded on silicon," Opt. Express **24**, 29941–29947 (2016).
13. C. Wang, C. Langrock, A. Marandi, M. Jankowski, M. Zhang, B. Desiatov, M. M. Fejer, and M. Lončar, "Ultrahigh-efficiency wavelength conversion in nanophotonic periodically poled lithium niobate waveguides," Optica **5**, 1438–1441 (2018).
14. K. Nassau, H. J. Levinstein, and G. M. Loiacono, "The domain structure and etching of ferroelectric lithium niobate," Appl. Phys. Lett. **6**, 228–229 (1965).
15. S. I. Bozhevolnyi, J. M. Hvam, K. Pedersen, F. Laurell, H. Karlsson, T. Skettrup, and M. Belmonte, "Second-harmonic imaging of ferroelectric domain walls," Appl. Phys. Lett. **73**, 1814–1816 (1998).
16. S. Kurimura and Y. Uesu, "Application of the second harmonic generation microscope to nondestructive observation of periodically poled ferroelectric domains in quasi-phase-matched wavelength converters," J. Appl. Phys. **81**, 369–375 (1997).
17. M. Flörsheimer, R. Paschotta, U. Kubitscheck, C. Brillert, D. Hofmann, L. Heuer, G. Schreiber, C. Verbeek, W. Sohler, and H. Fuchs, "Second-harmonic imaging of ferroelectric domains in LiNbO3 with micron resolution in lateral and axial directions," Appl. Phys. B **67**, 593–599 (1998).
18. P. Mackwitz, M. Rüsing, G. Berth, A. Widhalm, K. Müller, and A. Zrenner, "Periodic domain inversion in x-cut single-crystal lithium niobate thin film," Appl. Phys. Lett. **108**, 152902 (2016).
19. B. J. Rodriguez, R. J. Nemanich, A. Kingon, A. Gruverman, S. V. Kalinin, K. Terabe, X. Y. Liu, and K. Kitamura, "Domain growth kinetics in lithium niobate single crystals studied by piezoresponse force microscopy," Appl. Phys. Lett. **86**, 012906 (2005).
20. E. Soergel, "Visualization of ferroelectric domains in bulk single crystals," Appl. Phys. B **81**, 729–752 (2005).
21. S. Wang, V. Pasiskevicius, and F. Laurell, "High-efficiency frequency converters with periodically-poled Rb-doped KTiOPO4," Opt. Mater. **30**, 594–599 (2007).
22. G. Lindgren, A. Zukauskas, V. Pasiskevicius, F. Laurell, and C. Canalias, "Studies of sub-millisecond domain dynamics in periodically poled Rb-doped KTiOPO4, using online in situ second harmonic generation," Opt. Express **23**, 20332–20339 (2015).

Optics EXPRESS

23. M. Missey, S. Russell, V. Dominic, R. Batchko, and K. Schepler, "Real-time visualization of domain formation in periodically poled lithium niobate," Opt. Express **6**, 186–195 (2000).
24. S. Grilli, P. Ferraro, M. Paturzo, D. Alfieri, and P. De Natale, "In-situ visualization, monitoring and analysis of electric field domain reversal process in ferroelectric crystals by digital holography," Opt. Express **12**, 1832–1842 (2004).
25. H. Karlsson, F. Laurell, and L. K. Cheng, "Periodic poling of RbTiOPO4 for quasi-phase matched blue light generation," Appl. Phys. Lett. **74**, 1519–1521 (1999).
26. J. Hellström, R. Clemens, V. Pasiskevicius, H. Karlsson, and F. Laurell, "Real-time and in situ monitoring of ferroelectric domains during periodic electric field poling of KTiOPO4," J. Appl. Phys. **90**, 1489–1495 (2001).
27. C. Eigner, M. Santandrea, L. Padberg, M. F. Volk, C. E. Rüter, H. Herrmann, D. Kip, and C. Silberhorn, "Periodically poled ridge waveguides in KTP for second harmonic generation in the UV regime," Opt. Express **26**, 28827–28833 (2018).
28. P. O. Weigel, J. Zhao, K. Fang, H. Al-Rubaye, D. Trotter, D. Hood, J. Mudrick, C. Dallo, A. T. Pomerene, A. L. Starbuck, C. T. DeRose, A. L. Lentine, G. Rebeiz, and S. Mookherjea, "Bonded thin film lithium niobate modulator on a silicon photonics platform exceeding 100 GHz 3-dB electrical modulation bandwidth," Opt. Express **26**, 23728–23739 (2018).
29. G. D. Miller, "Periodically poled lithium niobate: modeling, fabrication, and nonlinear optical performance," Ph.D. thesis, Stanford University (1998).
30. G. Berth, V. Quiring, W. Sohler, and A. Zrenner, "Depth-resolved analysis of ferroelectric domain structures in Ti:PPLN waveguides by nonlinear confocal laser scanning microscopy," Ferroelectrics **352**, 78–85 (2007).
31. J. Kaneshiro, Y. Uesu, and T. Fukui, "Visibility of inverted domain structures using the second harmonic generation microscope: Comparison of interference and non-interference cases," J. Opt. Soc. Am. B **27**, 888–894 (2010).
32. S. Cherifi-Hertel, H. Bulou, R. Hertel, G. Taupier, K. D. H. Dorkenoo, C. Andreas, J. Guyonnet, I. Gaponenko, K. Gallo, and P. Paruch, "Non-Ising and chiral ferroelectric domain walls revealed by nonlinear optical microscopy," Nat. Commun. **8**, 15768 (2017).
33. S. Hell, G. Reiner, C. Cremer, and E. H. K. Stelzer, "Aberrations in confocal fluorescence microscopy induced by mismatches in refractive index," J. Microsc. **169**, 391–405 (1993).
34. E. Fatuzzo and W. J. Merz, *Ferroelectricity* (North-Holland, 1967).
35. L. Gui, H. Hu, M. Garcia-Granda, and W. Sohler, "Local periodic poling of ridges and ridge waveguides on X- and Y-Cut LiNbO3 and its application for second harmonic generation," Opt. Express **17**, 3923–3928 (2009).
36. S. Sanna and W. G. Schmidt, "LiNbO3 surfaces from a microscopic perspective," J. Phys. Condens. Matter **29**, 413001 (2017).
37. J. W. Choi, D. K. Ko, J. H. Ro, and N. E. Yu, "Sidewise domain wall velocity of MgO doped stoichiometric lithium niobate by real-time visualization," Ferroelectrics **439**, 13–19 (2012).
38. X. Huang, D. Wei, Y. Wang, Y. Zhu, Y. Zhang, X. P. Hu, S. N. Zhu, and M. Xiao, "Second-harmonic interference imaging of ferroelectric domains through a scanning microscope," J. Phys. D Appl. Phys. **50**, 485105 (2017).
39. D. E. Aspnes and A. A. Studna, "Dielectric functions and optical parameters of Si, Ge, GaP, GaAs, GaSb, InP, InAs, and InSb from 1.5 to 6.0 eV," Phys. Rev. B **27**, 985–1009 (1983).
40. D. Sandkuijl, A. E. Tuer, D. Tokarz, J. E. Sipe, and V. Barzda, "Numerical second- and third-harmonic generation microscopy," J. Opt. Soc. Am. B **30**, 382–395 (2013).
41. I. H. Malitson, "Interspecimen comparison of the refractive index of fused silica," J. Opt. Soc. Am. **55**, 1205–1209 (1965).
42. D. E. Zelmon, D. L. Small, and D. Jundt, "Infrared corrected Sellmeier coefficients for congruently grown lithium niobate and 5 mol. % magnesium oxide-doped lithium niobate," J. Opt. Soc. Am. B **14**, 3319–3322 (1997).
43. T. R. Volk, R. V. Gainutdinov, and H. H. Zhang, "Domain-wall conduction in AFM-written domain patterns in ion-sliced LiNbO3 films," Appl. Phys. Lett. **110**, 132905 (2017).
44. C. Godau, T. Kämpfe, A. Thiessen, L. M. Eng, and A. Haußmann, "Enhancing the domain wall conductivity in lithium niobate single crystals," ACS Nano **11**, 4816–4824 (2017).
45. J. T. Nagy and R. M. Reano, "Periodic poling of ion-sliced X-cut magnesium oxide doped lithium niobate thin films," in Conference on Lasers and Electro-Optics (Optical Society of America, 2018), paper SF2I.2.